AAPPS Bulletin

ORIGINAL ARTICLE

Open Access

Quantized fields induced topological features in Harper-Hofstadter model

Xue Han[1], Fude Li[1], De-Xiu Qiu[1], Kang Xue[1] and X. X. Yi[1,2*]

Abstract

Classical magnetic fields might change the properties of topological insulators such as the time reversal symmetry protected topological edge states. This poses a question that whether quantized fields would change differently the feature of topological materials with respect to the classical one. In this paper, we propose a model to describe topological insulators (ultracold atoms in square optical lattices with magnetic field) coupled to a tunable single-mode quantized field, and discuss the topological features of the system. We find that the quantized field can induce topological quantum phase transitions in a different way. To be specific, for fixed gauge magnetic flux ratio, we calculate the energy bands for different coupling constants between the systems and the fields in both open and periodic boundary conditions. We find that the Hofstadter *butterfly* graph is divided into a pair for continuous gauge magnetic flux ratio, which is different from the one without single-mode quantized field. In addition, we plot topological phase diagrams characterized by Chern number as a function of the momentum of the single-mode quantized field and obtain a quantized structure with non-zero filling factor.

Keywords: Quantized fields, Chern number, Topological features, Phase diagrams

1 Introduction

Since the observation of the quantized Hall effect [1], electronic topological quantum matter [2] became one of the most active subjects of condensed matter physics. The researchers have paid much attention to topological materials [3–7] including but not limited to Chern insulators (CIs) [8–12] in the past decades. Novel topological phases that correspond to different conducting edge or surface states are predicted and observed. Topological phase of matter exist not only in electronic systems but also in ultracold atomic gases in optical lattices [13–16]. The later system increases the modulation flexibility of topological materials and inspires a wide interest in topological insulators subject to external fields [17, 18], for instance, quantum quench [19, 20], thermalization [21, 22] and decoherence [23–25].

Manipulating the topological features of matter by coupling the systems to electromagnetic fields becomes an active research area for many years. Various topological structures coupled to electromagnetic fields are studied for different issues, including topological phases induced photocurrent [26–33], topological order by dissipation [34–36], and optical Hall conductivity [37–40]. Interestingly, classical electromagnetic fields can change the energy band structure of the topological materials and induce nontrivial topological edge states in topological insulators such as HgTe/CdTe quantum well [41] or graphene [42]. In addition, the superradiant phase transition occurs in quantum spin Hall insulator for arbitrary weak coupling between the system and fields [43]. This provides us with a new perspective to study the topological features of topological matter coupled to a quantized field. Many problems remain open, including how topological features can take place in a system where the topological tight-binding system coupled to a single-mode quantized field with momentum, and what is

*Correspondence: yixx@nenu.edu.cn

[2] Center for Advanced Optoelectronic Functional Materials Research, and Key Laboratory for UV Light-Emitting Materials and Technology of Ministry of Education, Northeast Normal University, 130024 Changchun, People's Republic of China
Full list of author information is available at the end of the article

the behavior of the Chern number in such a situation? We will answer these questions in this paper.

In this paper, we first introduce our framework that consists of the Harper-Hofstadter model and a single-mode quantized field. The Harper-Hofstadter model contains the Harpers model [44] and the Hofstadter model [45] for optical lattices, which is realizable in experiments [46, 47]. With the development of the Ultracold atoms, it has become an important platform for considering topological matter coupled to a quantized field, the experimental implementation of our scheme can be designed with several theoretical studies [48, 49]. In order to connect 1D and 2D physics, we express the model in a mixed real- and momentum-space called mixed-space representation [50–53]. With these arrangements, we calculate the energy bands of the quantized light-matter interaction system for both open and periodic boundary conditions. And then we calculate the Chern number of the system and show the topological quantum phase transitions induced by a single-mode quantized field. The changes of Chern number for fixed magnetic flux ratio indicate that the quantum field indeed can induce topological phase transition. Finally, we construct phase diagrams according to Chern number versus the single-mode quantized field to show all topological phases.

The paper is organized as follows. The Hamiltonian of Harper-Hofstadter model coupled to a single-mode quantized field is introduced in Sec. 2. Eigenspectrum of the system in hybrid representation is calculated and discussed in Sec. 3. The Chern number spectrum in periodic conditions is given in Sec. 4. Finally we conclude in Sec. 5.

2 Hamiltonian

2.1 The Harper-Hofstader model

We consider the Harper-Hofstader model, which describes the nearest-neighbor hopping of atoms in a square lattice. The system forms a cylinder with length N, circumference W and a uniform magnetic field is exerted. The Hamiltonian of the system is given by [44, 45]

$$\hat{H}_0 = -t \sum_{\langle i,j \rangle} \hat{c}_i^\dagger e^{i[\Phi_{ij} - \beta/W]\hat{I}} \hat{c}_j, \tag{1}$$

where $\hat{c}_i^\dagger = (\hat{c}_{i,\uparrow}^\dagger \; \hat{c}_{i,\downarrow}^\dagger)$ creates a fermion at site i in one of two internal states, pseudospin labeled by $\sigma = \{\uparrow, \downarrow\}$, $\langle i,j \rangle$ represents nearest neighbors, and t is the hopping amplitude. $\hat{I}$ stands for the identity matrix. Lattice plaquette Φ_{ij} depends on artificial vector potentials, and we employ the Landau gauge $\mathcal{A} = (0, \mathcal{A}_y, 0)$. Here, $\mathcal{A}_y = \Phi x = 2\pi\alpha x$, $\alpha = p/q$ (p and q are integers) is the magnetic flux per plaquette in units of flux quantum. The flux β pierce the cylinder along its height, which can be interpreted as an angle twisting the boundaries. Twist angles also can be used to define topological invariants [54]. We will average over β to reduce the effects of finite circumference W along the y-direction, and the boundary conditions are implemented via $\hat{c}_{N+1,y,\sigma} = 0$ and $\hat{c}_{x,W+1,\sigma} = \hat{c}_{x,1,\sigma}$ (finite sites N along the x-direction).

We consider nearest-neighbor hoppings on a two-dimensional square lattice with a cylinder boundary conditions along the y-direction as sketched in Fig. 1a. The horizontal direction is the direction along the cylinder, and the vertical one is around the cylinder. When the magnetic flux per plaquette α is not zero, the magnetic flux Φ accumulates due to jumping around the lattice as shown in Fig. 1b. The spectrum of the system versus lattice momentum $\mathbf{k}$ is shown in Fig. 1c. The periodicity of the bulk states is dictated by the denominator q and there are three bands in momentum space with $q = 3$. The boundaries of the magnetic Brillouin zone are at $k_y a \in (-\pi/3, \pi/3)$ and $k_x a \in (-\pi, \pi)$, where a is the lattice constant.

We start by writing the second quantization form of the Hamiltonian in Eq. (1) for a rectangular lattice in real space as

$$\hat{H}_0 = \sum_{\mathbf{r}} \hat{c}_{\mathbf{r}}^\dagger \hat{\mathbf{H}}_{\mathbf{r}} \hat{c}_{\mathbf{r}}. \tag{2}$$

Due to the chosen boundary conditions, the momentum along the y-direction is conserved while the momentum along x is not. Therefore, it is convenient to write the Hamiltonian in a mixed-space representation by taking the advantage of the conserved momentum along y. We write the annihilation operator by employing the Fourier transformation along y as

$$\hat{c}_{\mathbf{r}} = \frac{1}{\sqrt{N_y}} \sum_{k_y} e^{ik_y y} \hat{\Phi}_{m,k_y}, \tag{3}$$

where m represents the x coordinate in the two-dimensional lattice, and N_y represents the number of sites along y. In mixed-space representation, the Hamiltonian (1) becomes

$$\hat{H}_0 = \sum_{m,k_y} \hat{\Phi}_{m,k_y}^\dagger \hat{\mathbf{H}}_{m,k_y} \hat{\Phi}_{m,k_y}, \tag{4}$$

where $\hat{\Phi}_{m,k_y}^\dagger = (\hat{\Phi}_{m,k_y,\uparrow}^\dagger \; \hat{\Phi}_{m,k_y,\downarrow}^\dagger)$ creates fermion at (m, k_y). We write the details as shown in Appendix A (from Eqs. (27) to (30)).

2.2 The coupling of the Harper-Hofstader system with a quantized field

In this section, we focus on the coupling of the topological material with quantized fields. The light-matter interaction has been studied for various systems, which is a

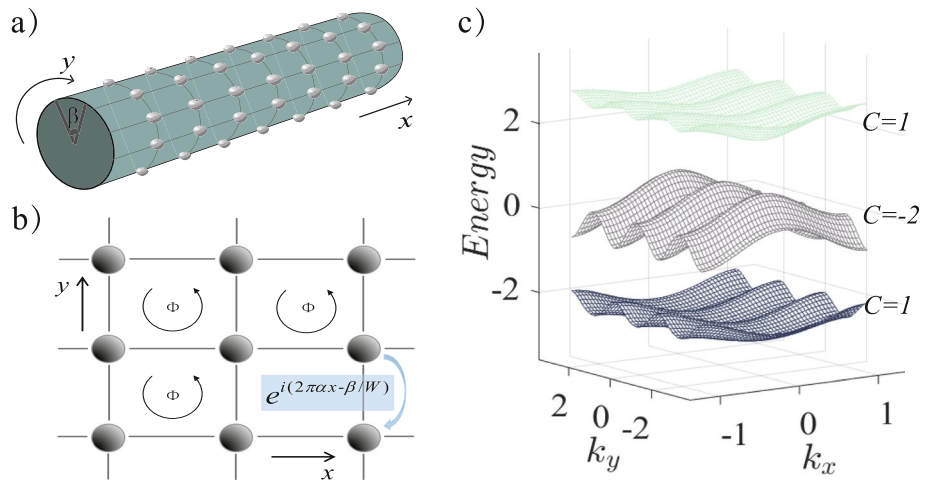

Fig. 1 Nearest-neighbor hopping of atoms in a square lattice with a uniform magnetic field. **a** Nearest-neighbor hopping on a two-dimensional square lattice with the periodic boundary conditions along the *y*-direction. **b** A partial view of the system. **c** The energy bands of the Harper-Hofstader model in momentum space, where the Chern numbers of three bands are 1, −2, 1. The parameters are $N = 30$, $a_x = a_y = t = 1$, $W = 9$, and $\beta = 0.2\pi$

fundamental tool of quantum physics in applications. For example, topological-enhanced nonreciprocal scattering [55], topological properties in the steady state with dissipation [56] and dissipative topological phase transition [36]. For simplicity, we do not consider decoherence of the single-mode field.

Consider a single-mode field with momentum $\mathbf{q}$ and frequency $\omega_{\mathbf{q}} = \nu\|\mathbf{q}\|$, where ν is the speed of light. The Hamiltonian of the single-mode field is given by

$$\hat{H}_l = \hbar\omega_{\mathbf{q}}\hat{b}^\dagger_{\mathbf{q}}\hat{b}_{\mathbf{q}}, \tag{5}$$

where $\hat{b}^\dagger_{\mathbf{q}}$ and $\hat{b}_{\mathbf{q}}$ are creation and annihilation operators, respectively. The Hamiltonian that describes the interaction between the system and the quantized fields may take the following form,

$$\hat{H}_I = -(\sum_{\mathbf{k}} g^*\hat{c}^\dagger_{\mathbf{k},\downarrow}\hat{b}^\dagger_{\mathbf{q}}\hat{c}_{\mathbf{k}+\mathbf{q},\uparrow} + \sum_{\mathbf{k}} g\hat{c}^\dagger_{\mathbf{k},\uparrow}\hat{b}_{\mathbf{q}}\hat{c}_{\mathbf{k}-\mathbf{q},\downarrow}), \tag{6}$$

where g is the effective atom-photon coupling constant [57, 58] and $\mathbf{q} = (k_T, 0, 0)$ represents the nonzero component k_T in x-direction. Experimentally, internal transitions between two atomic ground states (pseudospins) can be solved by utilizing Raman scattering processes [49, 59].

The coupling of the system (atoms) to the single-mode light field by Eq. (6) can be depicted in Fig. 2. The Hamiltonian in the real space is shown in Appendix B. The green and pink bars in Fig. 2a indicate the atoms in spin-up and spin-down states, respectively. The total transition path of photon (from gray atom to blue atom obliquely) is divided schematically into two continuous processes. The first process is regarded as the turnover of atoms with different pseudospins (from gray atom to blue atom vertically), and the second process is regarded as the momentum transition of atoms with the same pseudospin (from blue atom to blue atom horizontally). The above statements mean that k_T can be understood as a spin-dependent momentum transfer in the process.

With this consideration, we might rewrite the total effective Hamiltonian as $\hat{H}_{total} = \hat{H}_{\uparrow\uparrow} + \hat{H}_{\downarrow\downarrow} + \hat{H}_{\downarrow\uparrow} + \hat{H}_{\uparrow\downarrow} + \hat{H}_l$, which describes the whole system including lattice atoms and light field, see Fig. 2b. Here,

$$\hat{H}_{\uparrow\uparrow} = -2t\sum_{m,k_y}\{\cos[(\hat{k}_x + k_T)a] - \cos[(k_y + \mathcal{K}_y)a]\}\hat{\Phi}^\dagger_{m,k_y,\uparrow}\hat{\Phi}_{m,k_y,\uparrow}, \tag{7}$$

$$\hat{H}_{\downarrow\downarrow} = -2t\sum_{m,k_y}\{\cos[(\hat{k}_x - k_T)a] - \cos[(k_y + \mathcal{K}_y)a]\}\hat{\Phi}^\dagger_{m,k_y,\downarrow}\hat{\Phi}_{m,k_y,\downarrow}, \tag{8}$$

$$\hat{H}_{\uparrow\downarrow} = -g\sum_{m,k_y}\hat{\Phi}^\dagger_{m,k_y,\uparrow}\hat{b}_{\mathbf{q}}\hat{\Phi}_{m,k_y,\downarrow}, \tag{9}$$

$$\hat{H}_{\downarrow\uparrow} = -g^*\sum_{m,k_y}\hat{\Phi}^\dagger_{m,k_y,\downarrow}\hat{b}^\dagger_{\mathbf{q}}\hat{\Phi}_{m,k_y,\uparrow} \tag{10}$$

$\hat{H}_{\uparrow\downarrow}$ and $\hat{H}_{\downarrow\uparrow}$ stand for the processes of spin-flip. $\hat{H}_{\uparrow\uparrow}$ and $\hat{H}_{\downarrow\downarrow}$ represent the processes of momentum transfer. And $\mathcal{K}_y \equiv 2\pi\alpha m - \beta/W = eHx/\hbar c - \beta/W$, $eHx/\hbar c$ stands for the y-component of an artificial vector potential. It

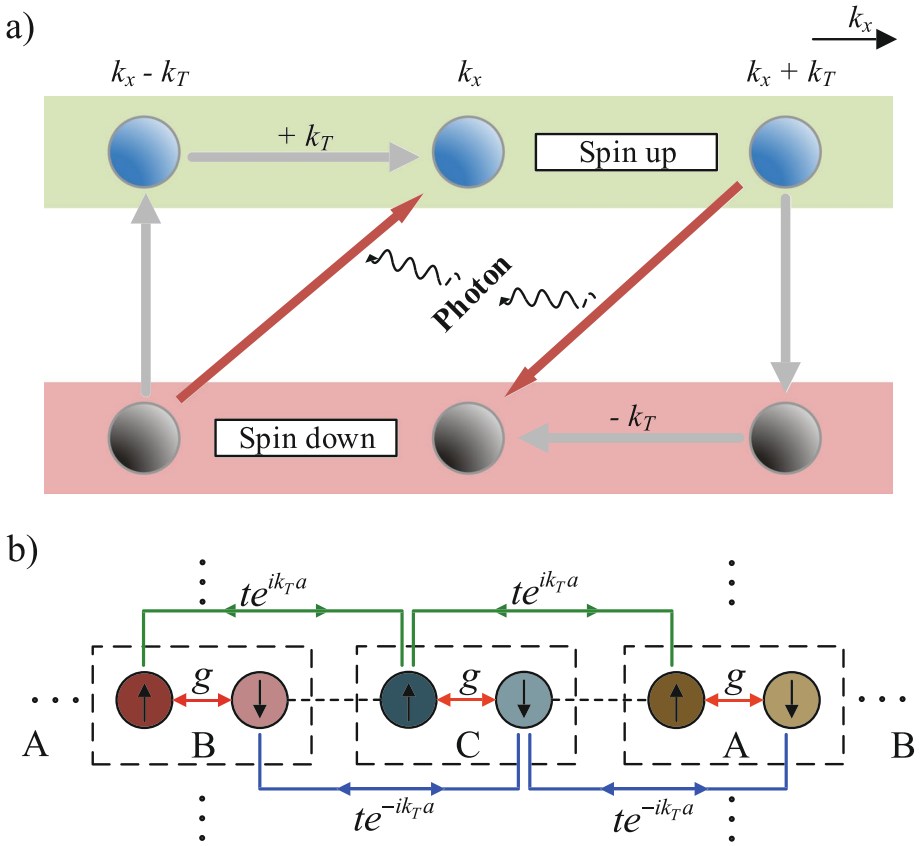

Fig. 2 **a** Schematic diagram of the coupling between the field (photon) and the system(atoms in the lattice). The blue and gray spheres represent atoms of spin up and spin down, respectively. **b** Schematic diagram of the coupling of pseudospins defined by $\hat{H}_{total}$ at $\alpha = 1/3$. The dashed rectangular box represents the coupling(red lines) between the pseudospins inside the lattice. The solid green and blue lines indicate the couplings of spin up and down between different lattices, respectively

may be generated by laser- assisted tunnelings [60, 61]. We also give the Hamiltonian of the first four parts in a real-space for more intuitive understanding. For details, see Appendix B (from Eqs. (32) to (35)).

We choose the basis as follows,

$$|\Psi_{m,k_y,\uparrow}\rangle = |\Phi_{m,k_y,\uparrow}\rangle \otimes |\{0\}\rangle, \tag{11}$$

and

$$|\Psi_{m,k_y,\downarrow}\rangle = |\Phi_{m,k_y,\downarrow}\rangle \otimes |\{1\}\rangle. \tag{12}$$

The implementation to realize a single-photon coupled to a single-site theoretically [62, 63]. With these settings, we express the matrix form of the Hamiltonian for the system in a mixed-space representation as

$$\hat{\mathbf{H}}_{total} = \begin{pmatrix} \varepsilon_{\uparrow}(\hat{k}) & -g \\ -g^* & \varepsilon_{\downarrow}(\hat{k}) + \hbar\omega_{\mathbf{q}} \end{pmatrix}, \tag{13}$$

where the diagonal elements represent spin-dependent kinetic energies and the off-diagonal terms stand for spin flips. The spin-up ($\uparrow$) kinetic energy is $\varepsilon_{\uparrow}(\hat{k}) = -2t\{\cos[(\hat{k}_x + k_T)a] + \cos[(k_y + \mathcal{K}_y)a]\}$, and the spin-down ($\downarrow$) kinetic energy is $\varepsilon_{\downarrow}(\hat{k}) = -2t\{\cos[(\hat{k}_x - k_T)a] + \cos[(k_y + \mathcal{K}_y)a]\}$, where a is the lattice spacing in the square lattice. The momentum shift k_T ($-k_T$) is corresponding to the $|\uparrow\rangle$ ($|\downarrow\rangle$) state along the x-direction. The matrix containing the momentum of light parameter $k_T a$ as phase factors is

$$\mathbf{J} = \begin{pmatrix} -t_x e^{ik_T a} & 0 \\ 0 & -t_x e^{-ik_T a} \end{pmatrix}. \tag{14}$$

The matrix indexed by position $x = ma$ is

$$\mathbf{D}_m = \begin{pmatrix} -2t\cos\theta_y & -g \\ -g^* & -2t\cos\theta_y + \hbar\omega_{\mathbf{q}} \end{pmatrix}, \tag{15}$$

where $\theta_y = (k_y + \mathcal{K}_y)a_y$, then Harper's Hamiltonian in mixed-space representation is given by

$$\begin{aligned}\hat{H}_{total} = &\sum_{m,k_y} \Psi^{\dagger}_{m,k_y} \mathbf{J}^{\dagger} \Psi_{m-1,k_y} \\ &+ \sum_{m,k_y} \Psi^{\dagger}_{m,k_y} \mathbf{D}_m \Psi_{m,k_y} \\ &+ \sum_{m,k_y} \Psi^{\dagger}_{m,k_y} \mathbf{J} \Psi_{m+1,k_y}.\end{aligned} \tag{16}$$

In the next section, we will discuss the effects of magnetic and single-mode fields on the eigenspectrums of the system.

3 Eigenspectrum

In this section, we first find the eigenspectrum of the Hamiltonian matrix in Eq. (16) and then express it as a function of the magnetic flux and the momentum of the single-mode field. We work in a cylindrical geometry with finite sites N along the x-direction as open boundaries, while periodic boundary conditions along the y-direction are considered. In this situation, the spin-dependent Harper's matrix

$$\hat{\mathbf{H}}_{total} = \begin{pmatrix} \mathbf{D}_{m-N/2} & \mathbf{J} & \cdots & \mathbf{0} & \mathbf{0} & \mathbf{0} & \mathbf{0} \\ \mathbf{J}^* & \ddots & \ddots & \mathbf{0} & \mathbf{0} & \mathbf{0} & \mathbf{0} \\ \vdots & \ddots & \mathbf{D}_{m-1} & \mathbf{J} & \mathbf{0} & \mathbf{0} & \mathbf{0} \\ \mathbf{0} & \mathbf{0} & \mathbf{J}^* & \mathbf{D}_m & \mathbf{J} & \mathbf{0} & \mathbf{0} \\ \mathbf{0} & \mathbf{0} & \mathbf{0} & \mathbf{J}^* & \mathbf{D}_{m+1} & \ddots & \vdots \\ \mathbf{0} & \mathbf{0} & \mathbf{0} & \mathbf{0} & \ddots & \ddots & \mathbf{J} \\ \mathbf{0} & \mathbf{0} & \mathbf{0} & \mathbf{0} & \cdots & \mathbf{J}^* & \mathbf{D}_{m+N/2} \end{pmatrix}, \tag{17}$$

has a tridiagonal block structure. The boundary condition in the x-direction is open, while there is a discrete translational invariance along the y-direction. The matrices $\mathbf{D}_m$, $\mathbf{J}$ and the null matrix $\mathbf{0}$ are square matrices of 2×2 dimension expanded by internal states $|\uparrow\rangle$ and $|\downarrow\rangle$. The total dimension of the matrix $\hat{\mathbf{H}}_{total}$ in Eq. (17) is $2N \times 2N$ because the size of the space along the x-direction is N.

In the following, we consider a size of the optical lattice to be 30 sites (a complete lattice period) along the x-direction as well as two spin states per site and periodic boundary conditions along the y-direction, so k_y is a good quantum number. The case analysis demonstrates that the eigenvalues E_{k_y} are labeled by a discrete band index n and momentum k_y, are also functions of the photon momentum k_T, electron-light coupling constant g, as well as flux ratio $\alpha = \Phi/\Phi_0$.

In Fig. 3, we show the spectrum of $\alpha = \Phi/\Phi_0$ versus the energy E_0 with $k_T = 0$. A standard *butterfly* graph in the case of zero photon momentum $k_T = 0$ and $g/t = 0$ is shown in Fig. 3a. For photon momentum $k_T = 1.2$ and $g/t = 0.5$, the standard *butterfly* graph split into two parts because the energy corresponding to the spin up and down is not the same as Fig. 3b shows.

We next discuss the case with flux ratio $\alpha = 1/3$, where 3 is the smallest integer denominator for the Hofstadter model exhibiting topological nontrivial bands [64]. We will analyze the eigenvalues E_{k_y} for different photon momentum k_T and coupling constant g. Let us first consider the case $k_T = 0$ and $g/t = 0$, the results are shown in Fig. 3c. We can clearly see three sets of degenerate bulk bands connected by spin-degenerate edge bands. The dashed lines indicate the edge bands and lines with a band shape indicate the bulk bands in Fig. 3c and d. The periodicity of bulk bands and the edge bands are $2\pi/3$ and 2π, respectively, along the k_y-direction as shown in Fig. 3c. The case of $k_T = 0.84$ and $g/t = 0.5$ as shown in Fig. 3d, it is the same as in Fig. 3b, which shows that the single-mode field leads to the separation of the energy spectrum. From Fig. 3d, we find six sets of bulk bands connected by edge states, which are subjected to photon momentum parameter k_T and coupling constant g. All the bulk bands have the same period of $2\pi/3$, while the edge bands are 2π along the k_y-direction. This means the boundaries of the magnetic Brillouin zone are at $k_y = \pm\pi/3$.

4 Chern numbers

In this section, we convert the cylindrical geometry into a torus one to study the Chern number spectrum, where periodic boundary conditions are imposed along the x and y directions. For rational $\alpha = 1/3$, we write the spin-dependent Harper's Hamiltonian as a 6×6 matrix in momentum (k_x, k_y) space

$$\mathbf{H}(k_x, k_y) = \begin{pmatrix} \mathbf{H}_{++} & \mathbf{H}_{+-} \\ \mathbf{H}_{-+} & \mathbf{H}_{--} \end{pmatrix}, \tag{18}$$

which defines 3×3 block matrices $\mathbf{H}_{--}$ or $\mathbf{H}_{++}$, where spin states $|\uparrow\rangle = |+\rangle$ and $|\downarrow\rangle = |-\rangle$. The spin-diagonal 3×3 block matrices

$$\mathbf{H}_{++} = \begin{pmatrix} \Gamma_1 & -e^{i(k_x+k_T)a} & -e^{-i(k_x+k_T)a} \\ -e^{-i(k_x+k_T)a} & \Gamma_2 & -e^{i(k_x+k_T)a} \\ -e^{i(k_x+k_T)a} & -e^{-i(k_x+k_T)a} & \Gamma_3 \end{pmatrix}, \tag{19}$$

$$\mathbf{H}_{--} = \begin{pmatrix} \Gamma_1 + \hbar\omega & -e^{i(k_x-k_T)a} & -e^{-i(k_x-k_T)a} \\ -e^{-i(k_x-k_T)a} & \Gamma_2 + \hbar\omega & -e^{i(k_x-k_T)a} \\ -e^{i(k_x-k_T)a} & -e^{-i(k_x-k_T)a} & \Gamma_3 + \hbar\omega \end{pmatrix}, \tag{20}$$

where $k_x + k_T$ and $k_x - k_T$ describe respectively the spin states $|\uparrow\rangle = |+\rangle$ and $|\downarrow\rangle = |-\rangle$ momentum transfer along the x direction. The kinetic energy terms are $\Gamma_m = -2\cos(k_y a - 2\pi\alpha m)$, with the magnetic flux ratio $\alpha = 1/3$ and m values (0, 1, 2).

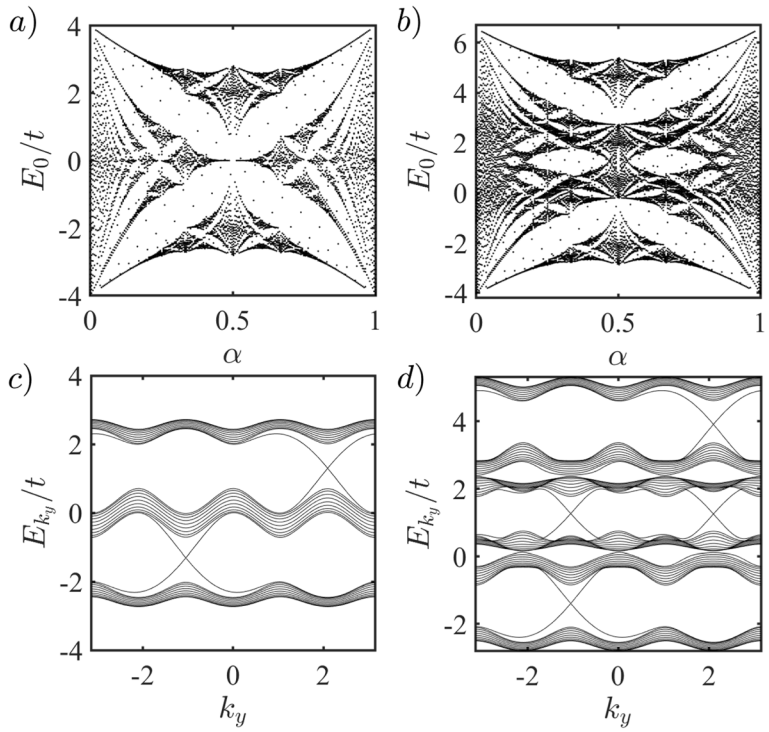

Fig. 3 The spectrum of the system with $\alpha = \Phi/\Phi_0$. **a** and **b** are for E_0 (in units of t). Eigenvalues E_{k_y} (in units of t) of the Harper's matrix Eq. (17) *vs* k_y for magnetic flux ratio $\alpha = 1/3, \beta = 0.2\pi, a = 1$, and $W = 9$ are shown in **c** and **d**. The parameters are **a** $k_T = 0$ and $g/t = 0$, **b** $k_T = 0.84$ and $g/t = 0.5$, **c** $k_T = 0$ and $g/t = 0$, and **d** $k_T = 0.84$ and $g/t = 0.5$

The spin-off-diagonal 3×3 block matrices are

$$\mathbf{H}_{+-} = \begin{pmatrix} -g & 0 & 0 \\ 0 & -g & 0 \\ 0 & 0 & -g \end{pmatrix}, \tag{21}$$

and $\mathbf{H}_{-+} = H^*_{+-}$. They describe spin-flip processes induced by the independently tunable single-mode field. The energy spectrum is shown in Fig. 5, which is similar to the cases with open boundary conditions, but there are no boundary states with periodic boundary conditions along the x and y directions. As a consequence, there is no edge state in the later case.

Next, we analyze the Chern spectrum with a single-mode quantized field and fixed flux ratio $\alpha = 1/3$. The energy spectrum associated with the Hamiltonian $\mathbf{H}(k_x, k_y)$ in Eq. (18) has six bands $E_{m_\sigma}(k)$ labeled by the band index m_σ (σ labels the spin). There are at least 2 band gaps when the bands are double degenerate, and there are at most 5 gaps when the system has no degeneracy. In the absence of overlapping regions between the energy bands $E_{m_\sigma}(k)$, the Chern number for the m_σ^{th} band is

$$C_{m_\sigma} = \frac{1}{2\pi i} \int_\Omega d^2k \mathcal{F}_{xy}^{(m_\sigma)}(k), \tag{22}$$

where the domain of integration Ω is the magnetic Brillouin zone. Namely, $\Omega_x = [-\pi, \pi]$ and $\Omega_y = [-\pi/q, \pi/q]$. The function

$$\mathcal{F}_{xy}^{(m_\sigma)}(k) = \frac{\partial A_y^{(m_\sigma)}(k)}{\partial_x} - \frac{\partial A_x^{(m_\sigma)}(k)}{\partial_y}, \tag{23}$$

is the Berry curvature expressed in terms of the Berry connection $A_j^{(m_\sigma)}(k) = \langle u_{m_\sigma}(k) | \partial_j | u_{m_\sigma}(k) \rangle$, where $|u_{m_\sigma}(k)\rangle$ are the eigenstates of the Hamiltonian $\mathbf{H}(k_x, k_y)$ defined in Eq. (18). In the limit of no electron-light coupling, $k_T = 0$ and $g = 0$, the energy spectrum for flux ratio $\alpha = p/q$ is doubly degenerate with q magnetic bands and $(q-1)$ gaps, such that the Chern number from Eq. (22) reduces to the standard form in the literature [64, 65]. To compute the Chern number C_{m_σ}, we generalize the discretization method used in the quantum Hall system [66, 67] without electron-light coupling $k_T = 0$ and $g = 0$. For this purpose, we define the link function

$$\mathcal{L}_j^{(m_\sigma)}(k) = \frac{\langle u_{m_\sigma}(k)|u_{m_\sigma}(k+\delta k_j)\rangle}{|\langle u_{m_\sigma}(k)|u_{m_\sigma}(k+\delta k_j)\rangle|},$$

and obtain the Berry curvature

$$\mathcal{F}_{xy}^{m_\sigma}(k) = \ln\left[\frac{\mathcal{L}_x^{m_\sigma}(k)\mathcal{L}_y^{m_\sigma}(k+\delta k_x)}{\mathcal{L}_x^{m_\sigma}(k+\delta k_y)\mathcal{L}_y^{m_\sigma}(k)}\right], \tag{24}$$

which is a purely imaginary number defined in the range of $-\pi \leq \mathcal{I}\left[\mathcal{F}_{xy}^{m_\sigma}(k)\right] \leq \pi$. The Chern number becomes

$$C_{m_\sigma} = \frac{1}{2\pi i}\sum_k \mathcal{F}_{xy}^{(m_\sigma)}(k). \tag{25}$$

When the energy bands $E_{m_\sigma}(k)$ overlap, we need to redefine the link variable of the degenerate bundle with degeneracy V via the multiplet $|\psi_{m_\sigma}^{(V)}(k)\rangle = \left[|u_{m_\sigma}^{(1)}(k)\rangle, \ldots, |u_{m_\sigma}^{(V)}(k)\rangle\right]$, leading to

$$\mathcal{L}_j^{(m_\sigma)}(k) = \frac{\mathrm{Det}\langle\psi_{\mathrm{m_\sigma}}^{(\mathrm{V})}(\mathrm{k})|\psi_{\mathrm{m_\sigma}}^{(\mathrm{V})}(\mathrm{k}+\delta\mathrm{k_j})\rangle}{|\mathrm{Det}\langle\psi_{\mathrm{m_\sigma}}^{(\mathrm{V})}(\mathrm{k})|\psi_{\mathrm{m_\sigma}}^{(\mathrm{V})}(\mathrm{k}+\delta\mathrm{k_j})\rangle|},$$

with these definitions, the expression for the Berry curvature defined in Eq. (24) remains valid when written in terms of the new link functions defined above. For two internal states and magnetic flux ratio $\alpha = p/q$, there is a maximum of $2q$ non-overlapping bands and a maximum of $2q$ Chern numbers.

Chern numbers are properties of bands $E_{m_\sigma}(k)$ or band bundles with degeneracy V and are independent of the location of the chemical potential μ. However, Chern numbers are defined only within band gaps and their values are dependent on the gap where the chemical potential locates. If the chemical potential μ is located in a band gap corresponding to the filling factor $\nu = r/2q$, then the Chern number is the sum of Chern numbers of bands with energies $E < \mu$

$$C_r = \sum_{m_\sigma, E<\mu}^{\nu=r/2q} C_{m_\sigma}. \tag{26}$$

Furthermore, via the bulk-edge correspondence [67], the Chern number C_r calculated from the torus geometry (bulk system without edges) measures the total chirality of edge states that are present in the gap for the cylindrical geometry.

In Fig. 4, Chern number C_r calculated from the torus geometry are shown as a function of photon momentum parameter k_T. It can be seen that the Chern numbers for $r = 1$ and $r = 5$ possess the same dependence on k_T. On the contrary, the Chern numbers for $r = 2$ shows the opposite dependence with respect to the case for $r = 4$.

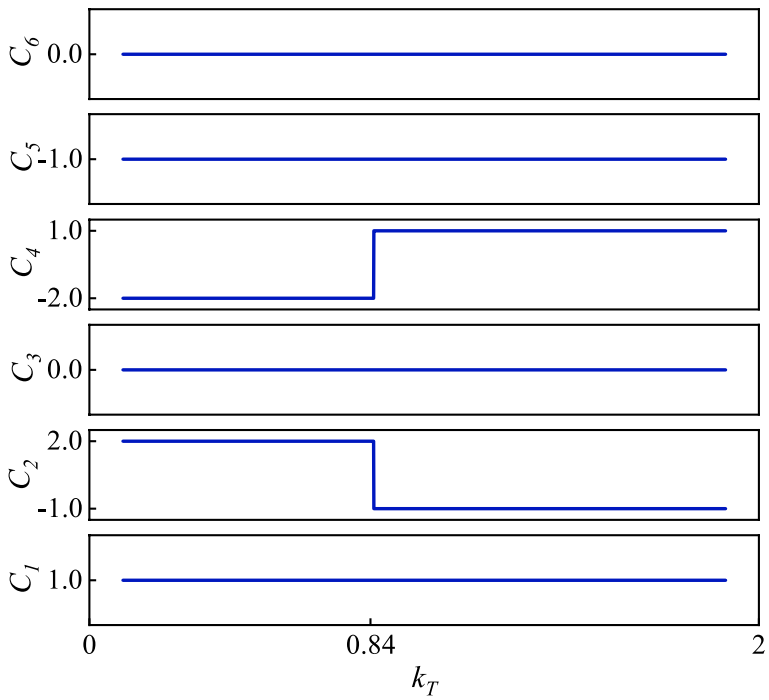

Fig. 4 Chern numbers C_r calculated from the torus geometry are shown for different filling factors $\nu = r/2q$ (r =1,2,3,4,5,6). Taking $r = 2$ as an example, it can be seen that a step change occurs at the critical point $k_T \sim 0.84$. The other parameters chosen are $\alpha = 1/3$, $\beta = 0.2\pi$, $a = 1$, $g = 0.5$, and $W = 9$

Considering the case of $r = 2$, the Chern number has a step change at the critical photon momentum $k_T \sim 0.84$. This indicates that the topology of the system changes at this point, and the system goes from one non-trivial topological phase to the other non-trivial topological phase as the momentum k_T increases.

Now, we are in order to analyze the connection between the band structures (Fig. 5) and the phases in Fig. 4. Energy bands as a function of k_T are shown in Figs. 5a–c, where Fig. 5a, b, and c correspond to different photon momentum $k_T = k_i$, $k_T = k_c$, and $k_T = k_f$, respectively. Taking $r = 2$ as an example, we need to examine only the second and the third bulk bands (arranged from the bottom to the top). Noticing that the energy of six bulk bands with $k_T = k_c$ possess touching points at the second and third bulk bands, i.e., the band gap is closed at $k_T = k_c$ for the second and third bulk bands, we then claim that the system with k_i is a non-trivial gaped phase, labeled by $C_2 = 2$ (see the green region in Fig. 5). While the system with k_f is a non-trivial phase which can be labeled by its Chern number $C_2 = -1$ (see the pink region in Fig. 5).

We show the enlarged energy corresponding to the edge states in the band gap between the second and the third bulk bands marked by the blue lines in Fig. 5d and e. Open boundaries are considered along the x direction, with L and R denoting the left and right boundaries, respectively. The green region with two pairs of chiral edge states and the Chern number 2 are shown respectively in Fig. 5d and 4c. The pink region with a pair of chiral edge states and Chern number -1 are shown in Fig. 5e and 4c, respectively.

The energy dispersions in x direction are similar to the case of periodic boundaries, the spectra (Fig. 5a and c) are plotted for comparison with the corresponding periodic cases (Fig. 5d and e). As the increase of the photon momentum k_T, the gap is closed and two pairs of chiral edge states disappear (Fig. 3d) at critical point k_c. This means the chiral edge states are merged into the bulk eigenstates, the gap opens, and a pair of chiral edge state appears again. In addition, the gapped phases for all k_T are characterized by the Chern number that determines the chiral edge states in agreement with the phase diagram.

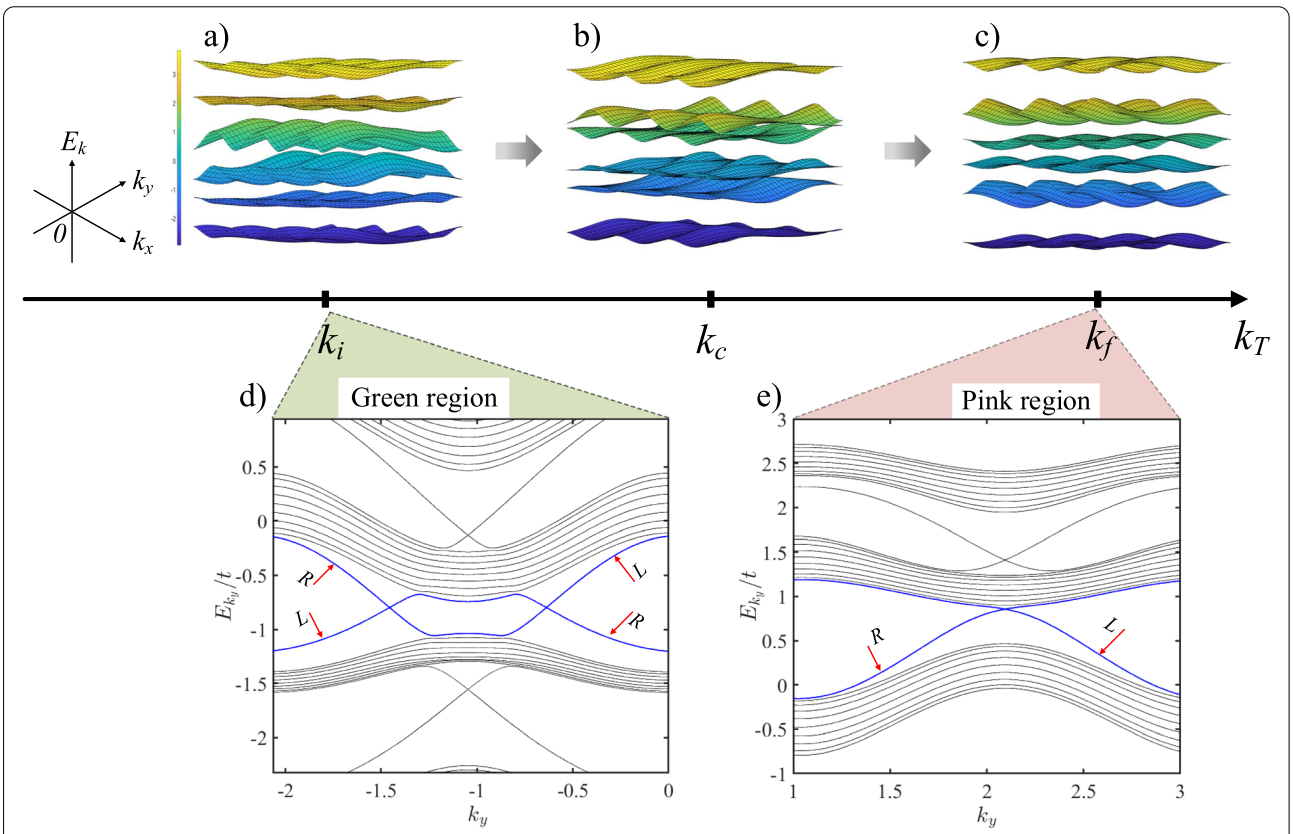

Fig. 5 Energy dispersions *vs* Bloch vector k with photon momentum k_T. k_i, k_c, and k_f are three special k_T chosen for **a**, **b**, and **c**, respectively. **d** and **e** are enlarged energy dispersion *vs* photon momentum k_T in order to illustrate edge bands and their location along x direction. The left and right boundaries are marked as L and R, respectively. The photon momentum chosen are in **a** and **d** $k_T = 0.3$, in **b** $k_T = 0.84$, and in **c** and **e** $k_T = 1.2$. Other parameters chosen are $\alpha = 1/3$, $\beta = 0.2\pi$, $a = 1$, and $W = 9$

Lastly, we discuss the mechanism of the topological phase transition induced by a quantized field in Fig. 2b. The coupling of the internal states of the site to the extra quantum field are characterized by the coupling strength g, this coupling leads to the splitting of a site on the lattice. The hopping between spin up and down in different lattices are described by a phase $te^{ik_T a}$ (or $te^{-ik_T a}$). In such a lattice model, modulating the momentum k_T is equivalent to adjusting the coupling strength of next-nearest neighbor hopping in the lattices, so that the topological structure of the lattice changes, which induces topological phase transition characterized by the changing of topological invariants (Chern number). In this sense, we conclude that the quantum field indeed can induce topological phase transition.

5 Conclusion

In conclusion, we have studied the topological features of an extended Harper-Hofstadter model which describes atoms in square optical lattices coupled to a single-mode quantized field. We have manipulated the topological features of matter by coupling the systems to quantized fields. The quantum light field is actually used to couple different atomic internal states to induce topological phase transition, which is different from the previous literature on coupling the internal states of atoms [68–70].

We calculated the energy band structure of the system and showed it as a function of the magnetic and single-mode quantized field. We find that the topological properties might be modulated by the single-mode quantized field, and topological quantum phase transitions could be induced by the single-mode quantized field. We have performed this analysis by computing the Chern number and comparing it with the case without quantized fields. Differences in the topological features of the system with and without a single-mode quantized field for fixed magnetic flux ratio are found and discussed. In addition, constructing phase diagrams by the Chern number and analyzing its dependence on the filling factor and the momentum of a single-mode quantized field, we found that Chern numbers are dramatically modified by the momentum of the single-mode quantized field.

Appendix A: The Hamiltonian $\hat{H}_0$

In this Appendix, we give the specific second quantization form of the Hamiltonian Eq. (1) in real space representation as

$$\hat{H}_0 = -t \sum_{<i,j>} \begin{pmatrix} \hat{c}^\dagger_{i,\uparrow} & \hat{c}^\dagger_{i,\downarrow} \end{pmatrix} \begin{pmatrix} e^{i(2\pi m\alpha-\beta/W)} & 0 \\ 0 & e^{i(2\pi m\alpha-\beta/W)} \end{pmatrix} \begin{pmatrix} \hat{c}_{j,\uparrow} \\ \hat{c}_{j,\downarrow} \end{pmatrix}, \quad (27)$$

We might rewrite the total Hamiltonian $\hat{H}_0 = \hat{H}_{\uparrow\uparrow} + \hat{H}_{\downarrow\downarrow}$ as

$$\hat{H}_{\uparrow\uparrow} = -\sum_{m,n} t\hat{c}^\dagger_{m,n,\uparrow}(\hat{c}_{m+1,n,\uparrow} + e^{i(2\pi m\alpha-\beta/W)}\hat{c}_{m,n+1,\uparrow}) + h.c. \quad (28)$$

$$\hat{H}_{\downarrow\downarrow} = -\sum_{m,n} t\hat{c}^\dagger_{m,n,\uparrow}(\hat{c}_{m+1,n,\downarrow} + e^{i(2\pi m\alpha-\beta/W)}\hat{c}_{m,n+1,\downarrow}) + h.c. \quad (29)$$

By employing the Fourier transformation along y-direction, the Eq. (27) in mixed-space representation as

$$\hat{H}_0 = -2t \sum_{m,k_y} \begin{pmatrix} \hat{\Phi}^\dagger_{m,k_y,\uparrow} & \hat{\Phi}^\dagger_{m,k_y,\downarrow} \end{pmatrix} \times \begin{pmatrix} \cos\hat{k}_x a - \cos[(k_y+\mathcal{K}_y)a] & 0 \\ 0 & \cos\hat{k}_x a - \cos[(k_y+\mathcal{K}_y)a] \end{pmatrix} \begin{pmatrix} \hat{\Phi}_{m,k_y,\uparrow} \\ \hat{\Phi}_{m,k_y,\downarrow} \end{pmatrix}, \quad (30)$$

where $\mathcal{K}_y = 2\pi\alpha m - \beta/W$.

Appendix B: The Hamiltonian $\hat{H}_{total}$

In this Appendix, we derive the Hamiltonian matrix given in Eq. 16. Firstly, we write the Eq. (6) in real space as

$$\hat{H}_I = -(g^* \sum_{m,n} e^{ik_T m}\hat{c}^\dagger_{m,n,\downarrow}\hat{b}^\dagger_{\mathbf{q}}\hat{c}_{m,n,\uparrow} + g\sum_{m,n} e^{-ik_T m}\hat{c}^\dagger_{m,n,\uparrow}\hat{b}_{\mathbf{q}}\hat{c}_{m,n,\downarrow}), \quad (31)$$

Then, we divide the jumping path after adding photons into two simultaneous path contributions as shown in Fig. 2. And we obtain the the following five parts in a real-space representation

$$\hat{H}_{\uparrow\uparrow} = -\sum_{m,n} t\hat{c}^\dagger_{m,n,\uparrow}(e^{ik_T a_x}\hat{c}_{m+1,n,\uparrow} + e^{i(2\pi m\alpha-\beta/W)}\hat{c}_{m,n+1,\uparrow}) + h.c. \quad (32)$$

$$\hat{H}_{\downarrow\downarrow} = -\sum_{m,n} t\hat{c}^\dagger_{m,n,\downarrow}(e^{-ik_T a_x}\hat{c}_{m+1,n,\downarrow} + e^{i(2\pi m\alpha-\beta/W)}\hat{c}_{m,n+1,\downarrow}) + h.c. \quad (33)$$

$$\hat{H}_{\uparrow\downarrow} = -\sum_{m,n} g\hat{c}^\dagger_{m,n,\uparrow}\hat{b}_{\mathbf{q}}\hat{c}_{m,n,\downarrow}, \quad (34)$$

$$\hat{H}_{\downarrow\uparrow} = -\sum_{m,n} g^*\hat{c}^\dagger_{m,n,\downarrow}\hat{b}^\dagger_{\mathbf{q}}\hat{c}_{m,n,\uparrow}, \quad (35)$$

$$\hat{H}_l = \hbar\omega_{\mathbf{q}}\hat{b}^\dagger_{\mathbf{q}}\hat{b}_{\mathbf{q}}. \quad (36)$$

Then we write the Hamiltonian matrix for ultracold atoms in a mixed-space representation as

$$\hat{\mathbf{H}} = \begin{pmatrix} \varepsilon_\uparrow(\hat{k}) & -g \\ -g^* & \varepsilon_\downarrow(\hat{k}) + \hbar\omega_{\mathbf{q}} \end{pmatrix}, \quad (37)$$

where the kinetic energy operator along the x direction is

$$\varepsilon_{\uparrow}(\hat{k}) = -2t\{\cos[(\hat{k}_x + k_T)a] + \cos[(k_y + \mathcal{K}_y)a]\}, \tag{38}$$

and the spin-down ($\downarrow$) kinetic energy is

$$\varepsilon_{\downarrow}(\hat{k}) = -2t\{\cos[(\hat{k}_x - k_T)a] + \cos[(k_y + \mathcal{K}_y)a]\}. \tag{39}$$

It is easily to find that $\hat{\mathbf{H}}$ consists of two matrices $\mathcal{T}$ and $\mathbf{D}_m$. The matrix indexed by position $x = ma$ is

$$\mathbf{D}_m = \begin{pmatrix} -2t\cos\theta_y & -g \\ -g^* & -2t\cos\theta_y + \hbar\omega_{\mathbf{q}} \end{pmatrix}, \tag{40}$$

where the kinetic energy operator of the system is given by according to Euler's formula

$$\mathcal{T} = \mathcal{T}_+(\hat{k_x}) + \mathcal{T}_-(\hat{k_x}), \tag{41}$$

with

$$\mathcal{T}_+(\hat{k_x}) = \begin{pmatrix} -t_x e^{ik_T a} e^{i\hat{k_x}a} & 0 \\ 0 & -t_x e^{-ik_T a} e^{i\hat{k_x}a} \end{pmatrix}, \tag{42}$$

and

$$\mathcal{T}_-(\hat{k_x}) = \begin{pmatrix} -t_x e^{-ik_T a} e^{-i\hat{k_x}a} & 0 \\ 0 & -t_x e^{ik_T a} e^{-i\hat{k_x}a} \end{pmatrix}. \tag{43}$$

The matrix containing the momentum of light parameter $k_T a_x$ as phase factors is

$$\mathbf{J} = \begin{pmatrix} -t_x e^{ik_T a} & 0 \\ 0 & -t_x e^{-ik_T a} \end{pmatrix}. \tag{44}$$

In mixed-space representation, we finally write Harper's Hamiltonian

$$\begin{aligned} \hat{H} = {} & \Sigma_{m,k_y} \Psi_m(k_y)^{\dagger} \mathbf{J}^{\dagger} \Psi_{m-1}(k_y) \\ & + \Sigma_{m,k_y} \Psi_m(k_y)^{\dagger} \mathbf{D}_m \Psi_m(k_y) \\ & + \Sigma_{m,k_y} \Psi_m(k_y)^{\dagger} \mathbf{J} \Psi_{m+1}(k_y). \end{aligned} \tag{45}$$

Acknowledgements
The authors thank Jianning Li for helpful discussions.

Authors' contributions
Xue Han developed the concept for the article, performed the literature search and numerical calculation. Fude Li and De-Xiu Qiu verified the accuracy of the calculation and corrected the grammar of the article. Kang Xue and X. X. Yi drafted and critically revised the work. All authors read and approved the final manuscript.

Funding
This work was supported by National Natural Science Foundation of China (NSFC) under Grants No.12175033 and No.12147206 and National Key R &D Program of China (No.2021YFE0193500).

Availability of data and materials
Data sharing not applicable to this article as no datasets were generated or analyzed during the current study.

Declarations

Ethics approval and consent to participate
Not applicable.

Consent for publication
Not applicable.

Competing interests
The authors declare that they have no competing interests.

Author details
[1]Center for Quantum Sciences and School of Physics, Northeast Normal University, 130024 Changchun, People's Republic of China. [2]Center for Advanced Optoelectronic Functional Materials Research, and Key Laboratory for UV Light-Emitting Materials and Technology of Ministry of Education, Northeast Normal University, 130024 Changchun, People's Republic of China.

Received: 11 September 2022 Accepted: 28 November 2022
Published online: 02 January 2023

References

1. K.V. Klitzing, G. Dorda, M. Pepper, New Method for High-Accuracy Determination of the Fine-Structure Constant Based on Quantized Hall Resistance. Phys. Rev. Lett. 45, 494 (1980)
2. C.-K. Chiu, J.C.Y. Teo, A.P. Schnyder, S. Ryu, Classification of topological quantum matter with symmetries. Rev. Mod. Phys. 88, 035005 (2016)
3. C.L. Kane, E.J. Mele, Quantum Spin Hall Effect in Graphene. Phys. Rev. Lett. 95, 226801 (2005)
4. C.L. Kane, E.J. Mele, Z_2 Topological Order and the Quantum Spin Hall Effect. Phys. Rev. Lett. 95(2005)
5. B.A. Bernevig, T.L. Hughes, S.-C. Zhang, Quantum Spin Hall Effect and Topological Phase Transition in HgTe Quantum Wells. Science 314, 1757 (2006)
6. M.Z. Hasan, C.L. Kane, Colloquium: Topological insulators. Rev. Mod. Phys. 82, 3045 (2010)
7. X.-L. Qi, S.-C. Zhang, Topological insulators and superconductors. Rev. Mod. Phys. 83, 1057 (2011)
8. F.D.M. Haldane, Model for a Quantum Hall Effect without Landau Levels: Condensed-Matter Realization of the "Parity Anomaly". Phys. Rev. Lett. 61, 2015 (1988)
9. X.-L. Qi, Y.-S. Wu, S.-C. Zhang, Topological quantization of the spin Hall effect in two-dimensional paramagnetic semiconductors. Phys. Rev. B 74, 085308 (2006)
10. T. Neupert, L. Santos, C. Chamon, C. Mudry, Fractional Quantum Hall States at Zero Magnetic Field. Phys. Rev. Lett. 106, 236804 (2011)
11. K. Sun, Z. Gu, H. Katsura, S. Das Sarma, Nearly Flatbands with Nontrivial Topology. Phys. Rev. Lett. 106, 236803 (2011)
12. E. Tang, J.-W. Mei, X.-G. Wen, High-Temperature Fractional Quantum Hall States. Phys. Rev. Lett. 106, 236802 (2011)
13. P. Hauke, M. Lewenstein, A. Eckardt, Tomography of Band Insulators from Quench Dynamics. Phys. Rev. Lett. 113, 045303 (2014)
14. D.-L. Deng, S.-T. Wang, L.-M. Duan, Direct probe of topological order for cold atoms. Phys. Rev. A 90, 041601 (2014)
15. A. Iurov, G. Gumbs, D. Huang, Peculiar electronic states, symmetries, and Berry phases in irradiated $\alpha - T_3$ materials. Phys. Rev. B 99(2019)
16. F.L.N. Santos, M.A. Caracanhas, M.C.O. Aguiar, R.G. Pereira, Bound states in two-dimensional Fermi systems with quadratic band touching. Phys. Rev. B 101, 155120 (2020)
17. X.-X. Zhang, T.T. Ong, N. Nagaosa, Theory of photoinduced Floquet Weyl semimetal phases. Phys. Rev. B 94, 235137 (2016)

18. T. Yoshida, K. Kudo, H. Katsura, Y. Hatsugai, Fate of fractional quantum Hall states in open quantum systems: Characterization of correlated topological states for the full Liouvillian. Phys. Rev. Research 2, 033428 (2020)
19. M.D. Caio, N.R. Cooper, M.J. Bhaseen, Quantum Quenches in Chern Insulators. Phys. Rev. Lett. 115, 236403 (2015)
20. J.H. Wilson, J.C.W. Song, G. Refael, Remnant Geometric Hall Response in a Quantum Quench. Phys. Rev. Lett. 117, 235302 (2016)
21. A. Rivas, O. Viyuela, M.A. Martin-Delgado, Density-matrix Chern insulators: Finite-temperature generalization of topological insulators. Phys. Rev. B 88, 155141 (2013)
22. D.P. Pires, D.O. Soares-Pinto, E. Vernek, Dynamics of quantum resources in regular and Majorana fermion systems. Phys. Rev. A 105, 042407 (2022)
23. H.Z. Shen, H. Li, Y.F. Peng, X.X. Yi, Mechanism for Hall conductance of two-band systems against decoherence. Phys. Rev. E 95, 042129 (2017)
24. S. Xu, H.Z. Shen, X.X. Yi, Current in an open tight-binding system. Phys. Rev. A 99, 012102 (2019)
25. V.V. Albert, B. Bradlyn, M. Fraas, L. Jiang, Geometry and Response of Lindbladians. Phys. Rev. X 6, 041031 (2016)
26. T. Oka, H. Aoki, Photovoltaic Hall effect in graphene. Phys. Rev. B 79, 081406 (2009)
27. O.V. Kibis, Metal-insulator transition in graphene induced by circularly polarized photons. Phys. Rev. B 81, 165433 (2010)
28. O.V. Kibis, O. Kyriienko, I.A. Shelykh, Band gap in graphene induced by vacuum fluctuations. Phys. Rev. B 84, 195413 (2011)
29. A. Camacho-Guardian, N. Goldman, P. Massignan, G.M. Bruun, Dropping an impurity into a Chern insulator: A polaron view on topological matter. Phys. Rev. B 99, 081105 (2019)
30. M.V. Durnev, S.A. Tarasenko, High-Frequency Nonlinear Transport and Photogalvanic Effects in 2D Topological Insulators. Ann. Phys. 531, 1800418 (2019)
31. R. Wang, B. Wang, R. Shen, L. Sheng, D.Y. Xing, Floquet Weyl semimetal induced by off-resonant light. EPL 105, 17004 (2014)
32. S. Vajna, B. Horovitz, B. Dóra, G. Zaránd, Floquet topological phases coupled to environments and the induced photocurrent. Phys. Rev. B 94, 115145 (2016)
33. L. Bucciantini, S. Roy, S. Kitamura, T. Oka, Emergent Weyl nodes and Fermi arcs in a Floquet Weyl semimetal. Phys. Rev. B 96, 041126 (2017)
34. J.C. Budich, P. Zoller, S. Diehl, Dissipative preparation of Chern insulators. Phys. Rev. A 91, 042117 (2015)
35. Y. Hu, P. Zoller, J.C. Budich, Dynamical Buildup of a Quantized Hall Response from Nontopological States. Phys. Rev. Lett. 117, 126803 (2016)
36. W. Nie, M. Antezza, Y.-X. Liu, F. Nori, Dissipative Topological Phase Transition with Strong System-Environment Coupling. Phys. Rev. Lett. 127, 250402 (2021)
37. T. Morimoto, Y. Hatsugai, H. Aoki, Optical Hall Conductivity in Ordinary and Graphene Quantum Hall Systems. Phys. Rev. Lett. 103, 116803 (2009)
38. J.G. Pedersen, M.H. Brynildsen, H.D. Cornean, T.G. Pedersen, Optical Hall conductivity in bulk and nanostructured graphene beyond the Dirac approximation. Phys. Rev. B 86, 235438 (2012)
39. H. Dehghani, A. Mitra, Optical Hall conductivity of a Floquet topological insulator. Phys. Rev. B 92, 165111 (2015)
40. T. Morimoto, Y. Hatsugai, H. Aoki, Optical Hall conductivity in 2DEG and graphene QHE systems. Physica E 42, 751 (2010)
41. N.H. Lindner, G. Refael, V. Galitski, Floquet topological insulator in semiconductor quantum wells. Nat. Phys. 7, 490 (2011)
42. T. Kitagawa, E. Berg, M. Rudner, E. Demler, Topological characterization of periodically driven quantum systems. Phys. Rev. B 82, 235114 (2010)
43. B. Gulácsi, B. Dóra, From Floquet to Dicke: Quantum Spin Hall Insulator Interacting with Quantum Light. Phys. Rev. Lett. 115, 160402 (2015)
44. P.G. Harper, Single Band Motion of Conduction Electrons in a Uniform Magnetic Field. Proc. Phys. Soc. Sect. A 68, 874 (1955)
45. D.R. Hofstadter, Energy levels and wave functions of Bloch electrons in rational and irrational magnetic fields. Phys. Rev. B 14, 2239 (1976)
46. M. Aidelsburger, M. Atala, M. Lohse, J.T. Barreiro, B. Paredes, I. Bloch, Realization of the Hofstadter Hamiltonian with Ultracold Atoms in Optical Lattices. Phys. Rev. Lett. 111, 185301 (2013)
47. C.J. Kennedy, W.C. Burton, W.C. Chung, W. Ketterle, Observation of Bose Einstein Condensation in a strong synthetic magnetic field. Nat. Phys. 11, 859 (2015)
48. F. Mivehvar, H. Ritsch, F. Piazza, Superradiant Topological Peierls Insulator inside an Optical Cavity. Phys. Rev. Lett. 118, 073602 (2017)
49. J.-S. Pan, X.-J. Liu, W. Zhang, W. Yi, G.-C. Guo, Topological Superradiant States in a Degenerate Fermi Gas. Phys. Rev. Lett. 115, 045303 (2015)
50. G. Ehlers, S.R. White, R.M. Noack, Hybrid-space density matrix renormalization group study of the doped two-dimensional Hubbard model. Phys. Rev. B 95, 125125 (2017)
51. J. Motruk, M.P. Zaletel, R.S.K. Mong, F. Pollmann, Density matrix renormalization group on a cylinder in mixed real and momentum space. Phys. Rev. B 93, 155139 (2016)
52. L. Stenzel, A.L.C. Hayward, C. Hubig, U. Schollwöck, F. Heidrich-Meisner, Quantum phases and topological properties of interacting fermions in one-dimensional superlattices. Phys. Rev. A 99, 053614 (2019)
53. L. Stenzel, A.L.C. Hayward, U. Schollwöck, F. Heidrich-Meisner, Topological phases in the Fermi-Hofstadter-Hubbard model on hybrid-space ladders. Phys. Rev. A 102, 023315 (2020)
54. Q. Niu, D.J. Thouless, Y.-S. Wu, Quantized Hall conductance as a topological invariant. Phys. Rev. B 31, 3372 (1985)
55. W. Nie, T. Shi, F. Nori, Y.-X. Liu, Topology-Enhanced Nonreciprocal Scattering and Photon Absorption in a Waveguide. Phys. Rev. Appl. 15, 044041 (2021)
56. M.J. Kastoryano, M.S. Rudner, Topological transport in the steady state of a quantum particle with dissipation. Phys. Rev. B 99, 125118 (2019)
57. G.-W. Lin, M.-Y. Ye, L.-B. Chen, Q.-H. Du, X.-M. Lin, Generation of the singlet state for three atoms in cavity QED. Phys. Rev. A 76, 014308 (2007)
58. E. G. Dalla Torre, J. Otterbach, E. Demler, V. Vuletic, M. D. Lukin, Dissipative Preparation of Spin Squeezed Atomic Ensembles in a Steady State. Phys. Rev. Lett. 110, 120402 (2013)
59. Y. Deng, J. Cheng, H. Jing, S. Yi, Bose-Einstein Condensates with Cavity-Mediated Spin-Orbit Coupling. Phys. Rev. Lett. 112, 143007 (2014)
60. M. Aidelsburger, M. Lohse, C. Schweizer, M. Atala, J.T. Barreiro, S. Nascimbne, N.R. Cooper, I. Bloch, N. Goldman, Measuring the Chern number of Hofstadter bands with ultracold bosonic atoms. Nat. Phys. 11, 162 (2015)
61. H. Miyake, G.A. Siviloglou, C.J. Kennedy, W.C. Burton, W. Ketterle, Realizing the Harper Hamiltonian with Laser-Assisted Tunneling in Optical Lattices. Phys. Rev. Lett. 111, 185302 (2013)
62. A. González-Tudela, C.S. Muñoz, J.I. Cirac, Engineering and Harnessing Giant Atoms in High-Dimensional Baths: A Proposal for Implementation with Cold Atoms. Phys. Rev. Lett. 122, 203603 (2019)
63. M. Lipka, M. Parniak, Single-Photon Hologram of a Zero-Area Pulse. Phys. Rev. Lett. 126, 063601 (2021)
64. D.J. Thouless, M. Kohmoto, M.P. Nightingale, M. den Nijs, Quantized Hall Conductance in a Two-Dimensional Periodic Potential. Phys. Rev. Lett. 49, 405 (1982)
65. M. Kohmoto, Topological invariant and the quantization of the Hall conductance. Ann. Phys. 160, 343 (1985)
66. T. Fukui, Y. Hatsugai, H. Suzuki, Chern Numbers in Discretized Brillouin Zone: Efficient Method of Computing (Spin) Hall Conductances. J. Phys. Soc. Jpn. 74, 1674 (2005)
67. Y.-S. Wu, *Lectures on Topological Aspects of the Quantum Hall Effect*, edited by H.C. Lee, Physics, Geometry and Topology (Plenum Press, New York, 1990), pp.461–491
68. Y. Yang, Z. Xu, L. Sheng, B. Wang, D.Y. Xing, D.N. Sheng, Time-Reversal-Symmetry-Broken Quantum Spin Hall Effect. Phys. Rev. Lett. 107, 066602 (2011)
69. W. Beugeling, N. Goldman, C.M. Smith, Topological phases in a two-dimensional lattice: Magnetic field versus spin-orbit coupling. Phys. Rev. B 86, 075118 (2012)
70. C. Hofrichter, L. Riegger, F. Scazza, M. Höfer, D.R. Fernandes, I. Bloch, S. Fölling, Direct Probing of the Mott Crossover in the SU(N) Fermi-Hubbard Model. Phys. Rev. X 6, 021030 (2016)

Publisher's Note